Collapse dynamics of two-dimensional dry and immersed granular columns of elongated grains

Nathan Coppin [1,*] Michel Henry,[1,†] Miguel Cabrera [2,‡] Emilien Azéma [3,4,§]
Frédéric Dubois [3,‖] Vincent Legat [1,¶] and Jonathan Lambrechts [1,#]
[1]*Institute of Mechanics, Materials and Civil Engineering, Applied Mechanics and Mathematics, UCLouvain, B-1348 Louvain-la-Neuve, Belgium*
[2]*Department of Geosciences and Engineering, Delft University of Technology, 2628CN Delft, Netherlands*
[3]*LMGC, Université de Montpellier, CNRS, Montpellier, France*
[4]*Institut Universitaire de France (IUF), Paris, France*

(Received 6 February 2023; accepted 28 August 2023; published 18 September 2023)

The collapse dynamics and runout of columns of elongated grains in two dimensions are numerically investigated in dry and immersed conditions, by means of an unresolved finite elements/discrete elements model. The elongated grains are modeled as rigid aggregates of disks. The column aspect ratio is systematically varied from 0.125 to 16 in order to span short and tall columns. To analyze the effect of the initial grain orientation, columns with an initial grain orientation that is either random or aligned with a given direction are both considered. Collapse dynamics, both in dry and immersed cases, are found analogous to that previously observed for circular grain columns, particularly with respect to the power law dependency for the runout as a function of the column aspect ratio. The effect of the fluid mainly results in a decrease of the runout distance. Interestingly, the collapse dynamics and runout are not significantly affected by the initial orientation of the grains, except maybe in the extreme case where the grains are all horizontally oriented, which geometrically prevents the collapse. Finally, a scaling based on the front propagation energy is proposed allowing one to unify the runout of short to tall and dry to immersed columns in a single description, regardless of the initial grain orientation.

DOI: 10.1103/PhysRevFluids.8.094303

I. INTRODUCTION

Granular materials behave at the boundary between fluids and solids. Ambient fluids can significantly impact their behavior, leading to hydrodynamic forces that compete with grain inertia [1–3]. As such, these materials play a governing role in geophysical flows [4,5], food processing silos [6], and chemical reactors [7], among others. Further adding to their complexity, there is a wide range of grain shapes that modify their collective shear strength by rate-dependent fabric and contact anisotropies [8–12]. Grain shapes can vary from concave and elongated grains to

*nathan.coppin@uclouvain.be
†michel.henry@uclouvain.be
‡m.a.cabrera@tudelft.nl
§emilien.azema@umontpellier.fr
‖frederic.dubois@umontpellier.fr
¶vincent.legat@uclouvain.be
#jonathan.lambrechts@uclouvain.be

convex grains, where interlocking and clustering is rapidly formed [10]. More specifically, elongated grains have been shown to align with the shear direction [13,14] and form growing clusters of aligned grains [15]. Given these complexities, the modeling of granular materials has attracted much interest from a wide range of disciplines [16,17]. Nevertheless, these approaches share a common simplification, focusing, to a greater extent, on the study of spherical and nearly-spherical materials [18].

An example of these approaches is the collapse of a granular column [19,20], recognized as a benchmark case for studying granular flows in dry, saturated, and immersed conditions [21–23]. In this configuration, a column of initial height H_0 and width L_0 is released and collapses under self-weight over a horizontal surface. After release, part of the column's potential energy is converted into kinetic energy and then dissipated until the column comes to rest and forms a deposit. The deposit runout L_f follows a piecewise power law as a function of the column aspect ratio H_0/L_0, allowing a differentiation between short and tall columns [19,20]. The fraction of dissipated energy increases with H_0/L_0 and is independent of surface or material parameters, like the grain size or the grain size distribution [19,20,24,25]. In addition, granular flows are strongly affected by the dilatant or contractant behavior defined by the system packing fraction, setting a clear distinction between initially dense and initially loose granular systems [26–28]. This dependency is unified in a simple scaling, requiring only the fluid-grain density ratio, proportional to the packing fraction, and the front kinetic energy for describing the system runout [27]. However, grain shapes that depart from spheres may modify, to some extent, the dependency on H_0/L_0 and on the initial density ratio [29–32]. For example, elongated grains show orientational features associated with a collective entanglement, or interlocking, that might prevent the column from collapsing [31,33] and yet form relatively loose granular systems or lead to the formation of ordered structures of aligned grains in the deposit that result in dense granular systems [33–35]. Nonetheless, for aspect ratios that are not sufficiently large to prevent the collapse, the influence of the grain shape on the collapse dynamics has been found to be small [33,36], except for particles with high blockiness (i.e., sharp edges that make them closer to polyhedra than to spheres) which have a reduced runout [18]. In the immersed case, most studies on elongated grains concentrate on colloidal suspensions of rods, which have similarities to polymer solutions and exhibit shear thinning due to orientational ordering [37,38]. For larger grains, the features specific to elongated grains are further amplified when surrounded by a fluid [35], but the extent to which they affect the mobility of granular flows is yet poorly understood, especially in the immersed case. The latter is, for example, of great interest in understanding the jamming of driftwood debris [39–41] or in the stability of layered cliffs which can result from debris or pyroclastic flows [42,43], where the collective orientation of its constituent grains plays a dominant role in the process.

In this work, we study the behavior of dry and immersed granular materials made of elongated grains, comparing initially disordered (i.e., a random initial grain orientation) and initially ordered (i.e., an initial grain orientation aligned with a given direction) systems. To that end, we explore the two-dimensional column collapse of elongated grains, employing a hybrid multiscale FEM-DEM framework (see Sec. II). Although constraining the degrees of freedom of the grains, the two-dimensional approach allows one to significantly reduce both the number of parameters to be studied and the computational cost. The objective is to describe the collapse dynamics of both dry and immersed columns of elongated grains that are far from interrupting the column collapse [31], with a particular focus on the orientation of the grains, its evolution, and its influence on the collapse. The two-dimensional approach reduces the grain orientation to a single scalar θ, helping to isolate its associated effects.

The studied collapses shed light on the distinct orientational features, at the scale of the grains, that are influenced by the ambient fluid, like grain clustering or grain reorientation, and that could modify the collapse sequence and thus its runout (see Secs. III and IV). The effect of grain orientation is then generalized in the description of the mobility of granular flows, suggesting the addition of a viscouslike term to the simplified scaling proposed by [27] (see Sec. V). Finally, conclusions and further effects of grain orientation are discussed in Sec. VI.

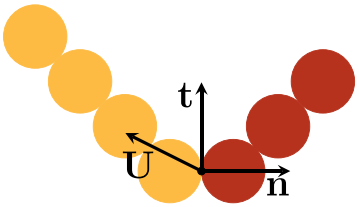

FIG. 1. Schematic of the interaction of two elongated grains, both consisting of a line cluster of disks. At the contact point ($b = 0$) the local frame of reference ($\mathbf{n}, \mathbf{t}$) and the relative contact velocity $\mathbf{U}$ are computed.

II. NUMERICAL METHOD

We use a hybrid multiscale finite element method coupled with a discrete element method (FEM-DEM framework) to simulate the coupled motion of fluid and grains during the column collapse. The open-source software MIGFLOW combines the insights from the grain physics with an affordable computational cost for solving the fluid phase [44]. Further details on the FEM-DEM framework can be found in [45]. The fluid phase is solved on a coarser scale with the volume-averaged Navier-Stokes equations [46], while the granular phase is solved on a finer scale with the nonsmooth contact dynamics [47,48]. The two scales are coupled through an interaction force between the fluid and granular phases. For the sake of computational convenience, both solvers are explicitly coupled. Hence the fluid solver evaluates the interaction force through a semi-implicit scheme [49], increasing the stability of the coupling.

The fluid fields are averaged within a control volume as a function of the granular medium porosity $\phi = 1 - V_g/V_T$, where V_g and V_T are the grains' volume and total control volume, respectively. This averaging allows the resolution of the fluid phase at a larger scale. Herein, the considered control volume corresponds to a mesh element. Hence the Navier-Stokes equations at this element become [46]

$$\frac{\partial \phi}{\partial t} + \nabla \cdot \mathbf{v} = 0, \tag{1}$$

$$\frac{\partial \rho_f \mathbf{v}}{\partial t} + \nabla \cdot \frac{\rho_f \mathbf{v}\mathbf{v}}{\phi} = \nabla \cdot \left[2\eta\phi\mathbf{d}\left(\frac{\mathbf{v}}{\phi}\right) - p\mathbf{I}\right] + \mathbf{f} + \phi\rho_f\mathbf{g}, \tag{2}$$

where $\mathbf{v}$ is the volume-averaged fluid velocity, ρ_f and η are the fluid density and viscosity, respectively, $\mathbf{d}$ is the deformation rate tensor, p is the fluid pressure, $\mathbf{I}$ is the identity tensor, $\mathbf{f}$ is the resultant of the fluid-grain interaction force tensor, and $\mathbf{g}$ is the acceleration due to gravity.

The granular material is solved with a nonsmooth contact dynamics (NSCD) approach [47,50]. The elongated grains are modeled as rigid clusters of disks. This implies that the bonds between the disks cannot be broken and are infinitely rigid, as the disks only serve a purely geometrical purpose in terms of contact detection and contact geometry. The mass, center of mass, and moment of inertia of a grain are computed according to the positions of its constituting disks. The positions and velocities of the grains are tracked through time and the contacts are solved based on momentum balances. This implicit approach allows for larger time steps and prevents grain interpenetration, which is useful for avoiding null porosities in the fluid elements. The NSCD approach starts with computing the grains' free velocities, ignoring the contacts between them, by means of Newton's second law and external forces such as the one due to $\mathbf{g}$. When a contact is detected, a local frame of reference and a relative velocity $\mathbf{U}$ are defined (see Fig. 1). Then, the contact is solved based on a local frictional contact law. This law follows the Signorini condition combined with a perfectly inelastic shock law in the normal direction and the Coulomb friction law in the tangent

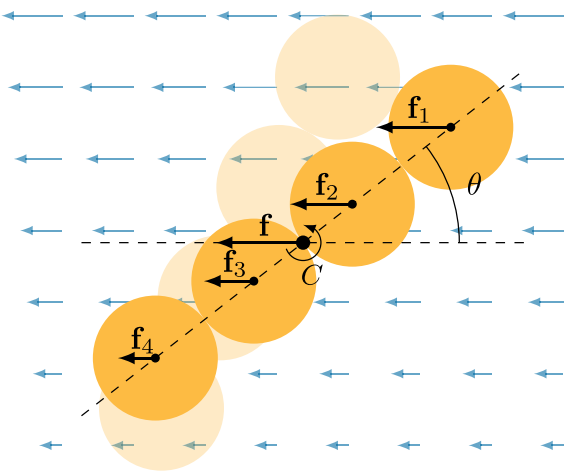

FIG. 2. Fluid forces exerted on disks in a shear flow and the resulting net force $\mathbf{f}$ and torque C on the corresponding elongated grain. The elongated grain has an orientation θ with respect to the horizontal. The transparent drawing indicates the consequent motion of the grain. The blue arrows represent the fluid velocity.

direction:

$$\text{If } b \leqslant 0: \qquad (3)$$
$$U_n^+ = 0, \quad R_n \geqslant 0, \quad U_n^+ R_n = 0,$$

$$|R_t| \leqslant \mu R_n, \quad |U_t^+| \neq 0 \Rightarrow R_t = -\mu R_n \frac{U_t^+}{|U_t^+|}, \qquad (4)$$

where the $+$ superscript indicates the value just after contact, μ the friction coefficient, b the distance between the two grains, and R_n and R_t the contact force normal and tangent components, respectively. Once R_n and R_t are determined, the grains' linear and angular velocities are adapted. At each time step, all contacts are to be solved at once. Since the resolution of one contact can influence other contacts in which any of the two grains are implied, the FEM-DEM framework uses a queue for iterating over the contacts until a convergence criterion is met. This criterion corresponds to the change in the velocity correction from the contact resolution between two iterations of the contact solver, multiplied by the time step [51]. In the present work, its value was set to 10^{-6}.

The fluid and grains interactions account for the pressure gradient and the drag. These interactions have been empirically adapted to take the Reynolds number and the porosity into account, so that they are valid for the fluid volume fractions and flowing regimes encountered in this work [52–54]. More details on the fluid-grain interaction force are presented in the Appendix.

Elongated grains are simulated as a single-line cluster of disks, as in [33], computing the fluid-grain interaction forces at the disk level. Hence the fluid forces acting on each disk are added into the resulting net force and torque on the elongated grain (see Fig. 2). This approach is similar to the one used by [55], in the simulation of fluidized beds of elongated grains. Note that these simplified two-dimensional hydrodynamic interactions on an elongated grain are inevitably different than those for three-dimensional rods. Nevertheless, we assume that they are still relevant for capturing the interplay between grains orientation and fluid kinematics.

We tested the current implementation of a line cluster of disks with the experimental observations of the free-fall kinematics of a single rod immersed in a fluid and within a planar setup [35]. Remarkably, the fluid-rod-like interactions, like fluttering and settling, are notably recovered by the fluid-grain system. Further improvements can be achieved by adding multiline clusters and by

correcting the surface of the grain so that it matches the one of the rod. However, in a large collection of grains such a surface correction could lead to a null porosity in a fluid element. For this reason, and for computational convenience, the simplest representation of a single line of disks was adopted for the study of grains orientation in a granular flow.

Simulation strategy

Taking inspiration from [35], the elongated grains are made of disks with a diameter $d = 2.15$ mm, with a density $\rho = 1840$ kg/m^3, and have a variable length l. Hence two collections of elongated grains are employed in this work, clustering three or four disks with the aim of obtaining an overall mean grain aspect ratio of $d/l = 3.21$. Moreover, a slight polydispersity of $1.05d$ on each grain was introduced for preventing crystallization. The friction coefficients were calibrated to $\mu_w = 0.3$ between the grains and the wall and $\mu_g = 0.9$ between grains, matching the results from [35] in terms of runout and deposit shape. In the immersed scenarios, the surrounding fluid is water with $\rho_f = 1000$ kg/m^3 and $\eta = 10^{-3}$ Pa s. For computational reasons, the mesh was finer near the initial column position and coarser at the other end of the domain. The most refined elements were $\approx$4.7 times the size of an elongated grain.

The samples were generated by depositing artificial disks under gravity and within a rectangular container. The artificial disks have diameters that correspond to the elongated grains' lengths. When the deposit comes to rest, the disks are replaced by the elongated grains with a desired orientation θ with respect to the horizontal. Their rotation is frozen and the grains settle. Then, their rotation is freed and the grains settle again, forming a two-dimensional axisymmetric column. To avoid grain size effects, the column's initial width is set to $L_0 = 0.29$ m, which is slightly larger than 75 times the grains' length [24]. The column is released by removing one of the container's lateral walls. For the sake of statistical significance, every configuration was simulated three times, resulting in 144 simulations. The maximum number of grains in a simulation was 89 000. The studied dry column collapses are in the free-fall regime and the immersed columns are in the inertial regime according to [1]. Therefore, the grains inertia are expected to control the flow.

The simulations are divided into two groups. The first group of simulations focuses on the general dynamics of a column collapse of initially disordered elongated grains (i.e., grains randomly oriented) in dry and immersed conditions. The initial disordered column is set as a random distribution of elongated grains with initial orientation within a full rotation ($0^\circ \leqslant \theta \leqslant 360^\circ$). The initial porosity for this stage is uniform across the column, with $\phi = 0.237 \pm 0.014$. The column aspect ratio was increased from $H_0/L_0 = 0.125$ to $H_0/L_0 = 16$, exploring the transition from short to tall columns. In the second group of simulations, a short and a tall column are studied ($H_0/L_0 \in [0.5; 8]$), exploring the effect of ordered grains (i.e., columns having all grains preferentially oriented in a given direction) with the main initial orientations $\theta_0^* \in [-90^\circ; -60^\circ; -45^\circ; -30^\circ; 0^\circ; 30^\circ; 45^\circ; 60^\circ; 90^\circ]$. Note that columns with a main orientation of $\theta_0^* < 0^\circ$ have a tendency to lean on the left wall. In this stage, the resulting porosity range is $\phi = 0.207 \pm 0.017$. Therefore, it can be argued that dense columns are studied in both stages.

III. COLUMN COLLAPSE OF RANDOMLY ORIENTED ELONGATED GRAINS

The column collapse of elongated grains shows a similar sequence as that of collapses involving spherical or nearly spherical grains [21–23]. This sequence initiates with an accelerating phase where the grains free fall or move laterally [see Figs. 3(c) and 3(d)], then transition to a predominant side-propagation phase [see Figs. 3(e) and 3(f)], and finally a decelerating phase until forming a deposit [see Figs. 3(g) and 3(h)]. Here, the collapse sequence duration is normalized by a reference dimensionless time $\tau = \sqrt{2H_0/g^*}$, accounting for the relative free-fall time of a grain from the initial height of the column H_0 and with $g^* = g\frac{\rho - \rho_f}{\rho}$ as the effective gravity correcting for buoyancy [56,57]. Movies of the column collapses presented in this work are available as Supplemental Material [58].

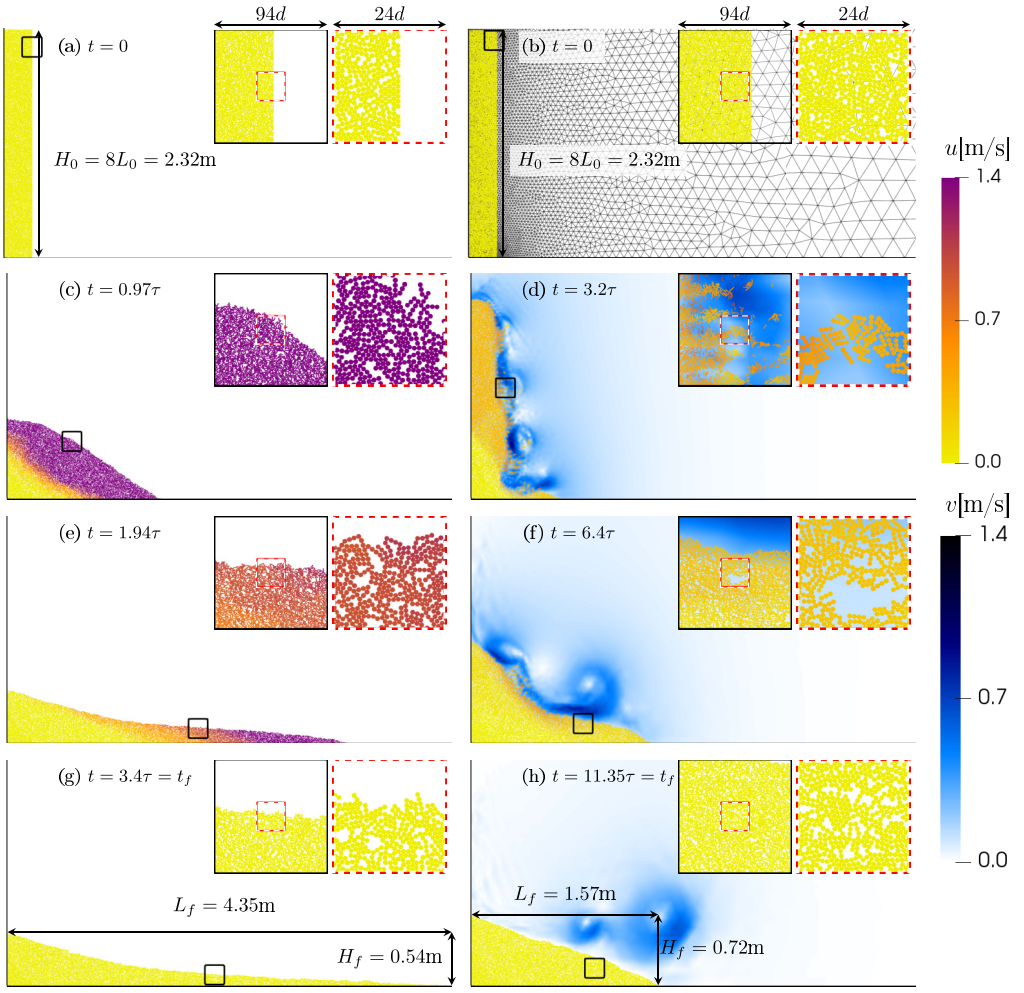

FIG. 3. Snapshots of a dry [(a),(c),(e),(g)] and immersed [(b),(d),(f),(h)] column collapse with initial aspect ratio $H_0/L_0 = 8$ and random initial grain orientation. The grains and fluid elements are colored with their instantaneous velocity u and v, respectively. The insets correspond to zooms on the column region marked with the same border pattern.

Interestingly, a clear distinction between dry and immersed column collapses is observed on the released volume at the initiation phase and the velocity at which it propagates. In dry columns almost all moving grains are in motion after initiation, while in immersed columns only a thin vertical layer, next to the release face, starts moving and propagates inwards during collapse. This localised mobilization is not surprising, being observed in the collapse of dense columns [27,28] and attributed to the competing action of the grains tendency to dilate and the fluid infiltration. This pore pressure effect [59] is well captured by the current numerical model, as the pressure is lower inside the grains when the columns start to collapse. As a result of the corresponding fluid motion, the observed contact forces between the grains are more important in the immersed case with respect to the apparent gravity. Moreover, in immersed columns, the grains near the free surface form fingerlike structures perpendicular to the moving mass [see Figs. 3(d) and 3(f)]. As these structures accelerate, they cross each other and recirculate with the so-induced vortices in the fluid. This dynamic is similar to the one of interacting Stokes clouds [45]. As they reach the

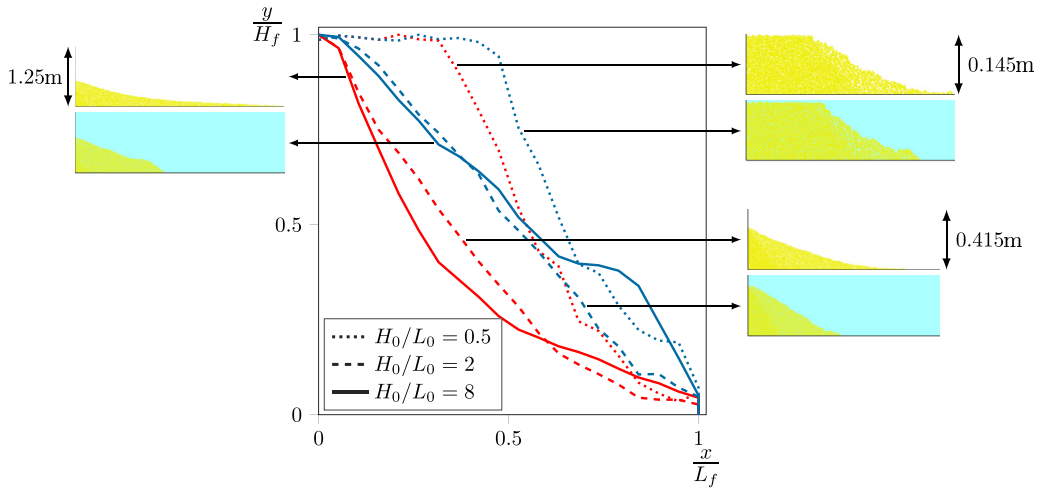

FIG. 4. Dimensionless deposit profiles for different column aspect ratios H_0/L_0. The red and blue colors indicate dry and immersed collapses. The insets show snapshots of the corresponding profiles. The light blue backgrounds indicate the immersed cases.

bottom surface, they accumulate and form a concave surface behind the flow front. The concave surface deflects the flow upwards, similar to a hydraulic ski jump [60], and sets the grains to deposit halfway from L_0. At the deceleration phase, the flow limits to a region near the free surface. Tall columns form a concave deposit shape in dry collapses and a roughly triangular shape in immersed collapses, as a result of the smoothing induced by the remaining vortices in the fluid (see Fig. 4).

Note that some bumps due to the hydraulic ski jump behavior can appear in the final deposit shape for immersed collapses. The differences between dry and immersed collapses vanish for short columns, as in that case the motion only takes place in a wedge in the upper right corner of the column.

The collapse sequence can be captured by following the released mass front position L (see Fig. 5, left). It should be noted that avalanches are transient in nature and that a steady state in the side-propagation phase does not really occur, but rather an inflexion from acceleration to deceleration [61]. Nevertheless, the average velocity U^{fr} of the front position L can be defined as a characteristic of the side-propagation phase, averaging the slope of the curve in Fig. 5 between the times at which 30% and 70% of the final runout are reached. From this, the front kinetic energy can also be defined as $E_k^{fr} = MU^{fr2}/2$, with M as the column total mass. Moreover, in the presence of a fluid, multiple collapse phases can be observed, as in [62] for saturated columns, but their reproducibility between the simulations is low.

The runout time t_r and the final collapse time t_f are defined as the elapsed time until $L = L_f$ and as the elapsed time until the grains come to rest, respectively (see Fig. 5, left). Both t_r and t_f are found to vary with the ambient fluid and with the column initial aspect ratio H_0/L_0, leading to longer collapses in the immersed cases (see Fig. 5, right). In dry columns, t_r/τ is nearly constant, indicating a free-fall regime independent of H_0/L_0. The value of t_f/τ first increases as more grains are available to flow on the free surface of the deposit without increasing the runout. After a maximum at $H_0/L_0 = 1$, indicating a transition from short to tall columns, t_f/τ gets closer to t_r/τ as the motion localizes in a shallow flowing layer at the front. In the immersed case, both t_r/τ and t_f/τ increase with H_0/L_0 as the grain motion is hindered by the fluid phase. The difference between them also increases as the fluid motion is more important and is able to sustain grain motion at the free surface of the deposit for a longer time. As the columns get taller, the fingerlike structures start to appear. These clusters of grains can have a larger settling velocity than isolated grains [63], which could explain

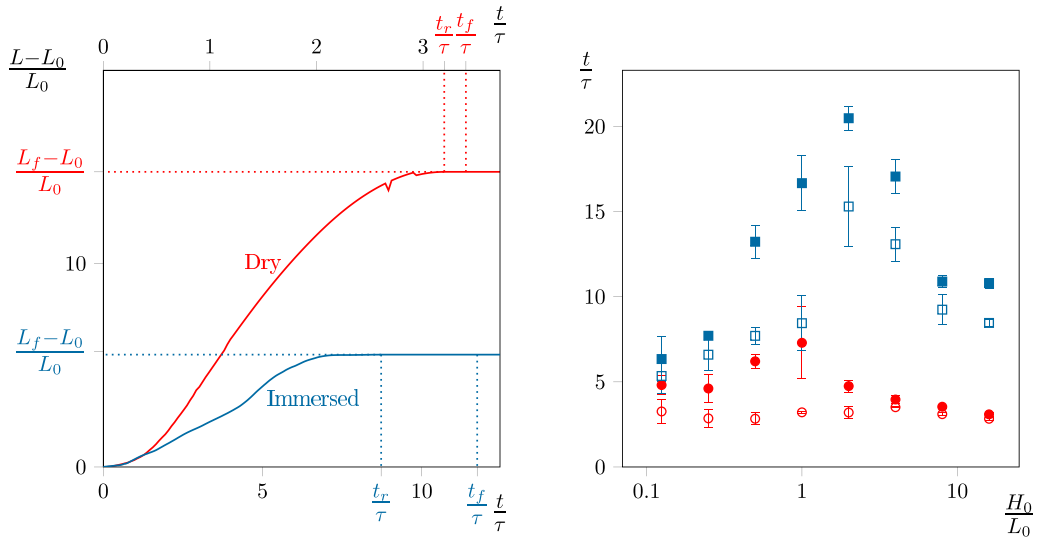

FIG. 5. Left: temporal evolution of the normalized front position during the collapse for a column of aspect ratio $H_0/L_0 = 8$. The dotted lines indicate the dimensionless runout t_r/τ and final t_f/τ times relative to the normalized runout $(L_f - L_0)/L_0$. Right: dimensionless runout t_r/τ (empty symbols) and final t_f/τ (solid symbols) times as a function of H_0/L_0. The red circles and the blue squares indicate dry and immersed collapses, respectively.

the associated decrease of both t_r/τ and t_f/τ. This time, the difference between them decreases, as the fluid motion is even more important and is able to push the grains forward.

As mentioned above, a characteristic of the column collapse is the distinction between short and tall columns. These collapse types follow a piecewise power law for the normalized runout $(L_f - L_0)/L_0$, increasing with H_0/L_0 and being steeper for the case of short columns. Here, the distinction between short and tall columns is also observed (Fig. 6, left), which is independent of the employed grain shape ratios ($d/l \approx 3$). The transition between short and tall columns is not exactly identified but occurs for H_0/L_0 somewhere between 2 and 4 for the dry case and between 1 and 2 for the immersed case. Moreover, the normalized deposit final height H_f/H_0 also follows a piecewise power law (see Fig. 6, right). The transition occurs at $H_0/L_0 = 1$ in both cases, resulting in a lower slope for the immersed case. This is due to the fluid preventing the grains from sliding too far and hence, by mass conservation, leading to higher final heights.

The grain orientation is tracked during the collapse, focusing on the main orientation and corresponding anisotropy of the moving grains. Let $\mathbf{s}_n = [\cos(\theta_n), \sin(\theta_n)]$ be the orientation vector of the grain n parallel to its longest dimension, with θ_n as the corresponding angle with respect to the horizontal. Since keeping track of the orientation of each grain is too complex and demanding, the focus is set on the probability density function $P(\theta) = N_\theta/\delta\theta$, such as N_θ is the number of grains with orientation between $[\theta - \delta\theta/2; \theta + \delta\theta/2]$ and $\theta \in [-90^\circ; 90^\circ]$. This periodic distribution can be approximated with the first two terms of its Fourier series expansion [64]:

$$P(\theta) = \frac{1}{2\pi}\{1 + a\,\cos[2(\theta - \theta^*)]\}, \tag{5}$$

where θ^* is the main orientation and a describes the anisotropy of the distribution. Furthermore, the values θ^* and a are computed from a so-called fabric tensor [9,65]:

$$S_{ij} = \frac{1}{N}\sum_n s_n^i s_n^j, \tag{6}$$

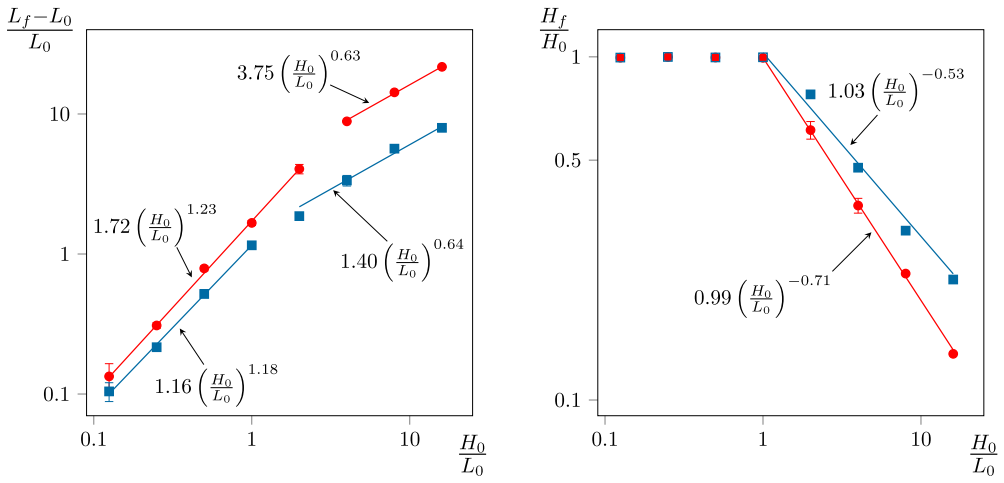

FIG. 6. Normalized runout (left panel) and normalized final height (right panel) for columns with randomly oriented grains as a function of the column aspect ratio H_0/L_0. The red circles and the blue squares indicate dry and immersed collapses, respectively. Error bars correspond to one standard deviation. Note that some of the error bars are sufficiently small so that they cannot be distinguished.

with N as the total number of grains. The anisotropy a can then be obtained as $2(S_1 - S_2)$, with S_1 and S_2 the principal values of $\mathbf{S}$ and the main orientation θ^* as the orientation of the first principal direction of $\mathbf{L}$. For consistency, these quantities focus on the moving grains, excluding all grains that moved less than a distance d between $t \in [0 : t_f]$.

The time evolution of θ^* and a of a typical column collapse sequence is shown in Fig. 7. Here, the initial random orientation is slightly anisotropic and aligned along the horizontal, which comes from the sample generation process driven by gravity deposition [66]. After the collapse starts, the

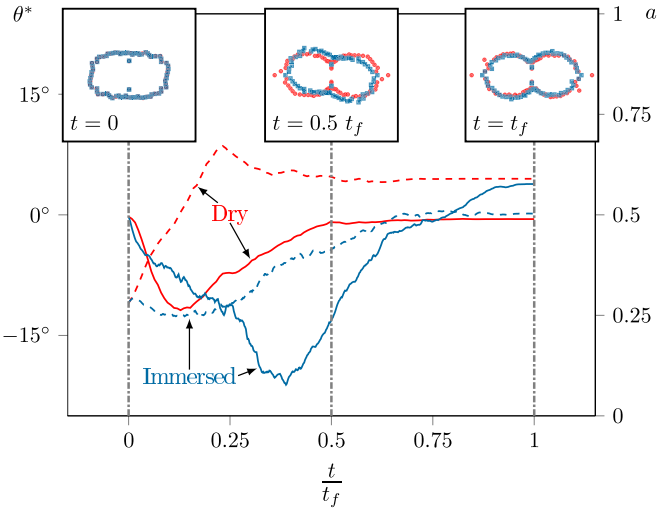

FIG. 7. Temporal evolution of the main orientation θ^* (solid) and anisotropy a (dashed) of the orientation distribution for a random initial orientation and $H_0/L_0 = 8$. The red and blue colors indicate dry and immersed collapses. The insets are polar plots of the orientation distribution showing the relative frequency of a given orientation.

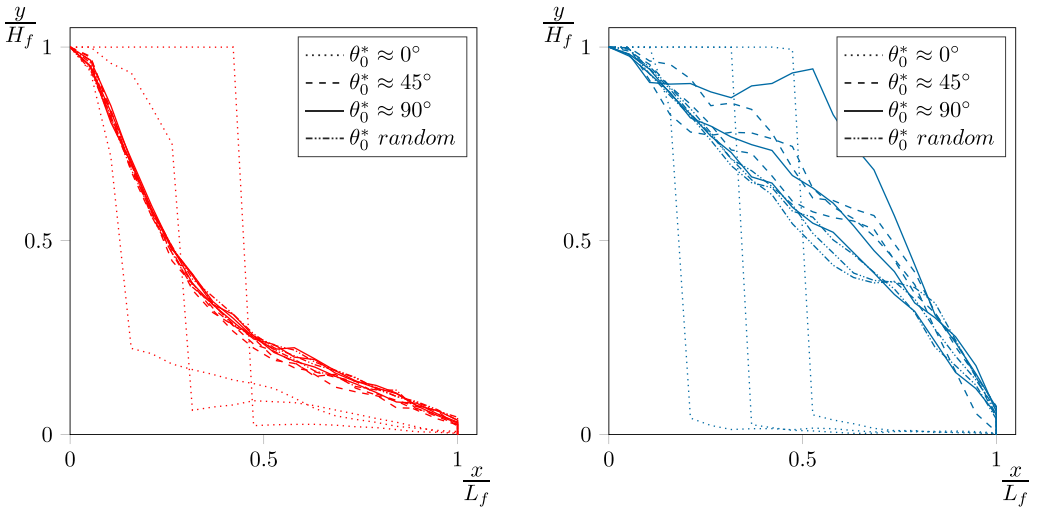

FIG. 8. Dimensionless deposit profiles for different initial grain main orientations θ_0^* in the dry (left, in red) and immersed (right, in blue) cases. The columns have an aspect ratio $H_0/L_0 = 8$.

grains align with the granular flow direction, changing from nearly $-10°$ in dry flows and $-20°$ in immersed flows to then nearly horizontal orientations (instants II and III in Fig. 7). Overall, the moving grains' anisotropy increases with time, having a steeper increase in dry collapses. In dry columns, the orientation of the grains stagnates halfway to the end of the flow, while in immersed columns, the grains' orientation changes during the whole collapse duration. This is because in dry flows the grains' motion localizes more rapidly into a shallow flowing layer, while in immersed flows the fluid vortices keep interacting with the grains even after the formation of the shallow flowing layer. Note that the final values of θ^* and a are similar for both cases, reaching a state often referred to as a nematic configuration [34,35].

IV. COLUMNS WITH AN INITIAL GRAIN ORIENTATION

This section focuses on exploring the effect of the initial main grain orientation ($\theta_0^* \in [-90° : 90°]$) in short and tall columns ($H_0/L_0 = [0.5, 8]$), respectively. The collapse dynamics, the runout, and the evolution of θ^* are compared to the random case that was explored in the previous section.

Overall, when a column collapse takes place ($\theta_0^* \neq 0°$), the initial grain orientation does not modify the collapse sequence described in Sec. III. However, for the metastable case of $\theta_0^* = 0°$, i.e., a "brick-wall" configuration, only a few grains are released from the column, forming a steplike deposit (see the dotted profiles in Fig. 8). In addition to this, in immersed tall column collapses, with $\theta_0^* \neq 0°$, the bumps can be more important (see Fig. 8). Moreover, columns with main grain orientations ($\theta_0^* \neq [0°; 90°]$) tend to slide in stacked clusters of grains, reaching a longer runout when the main grain orientation favors the slide at release ($\theta_0^* < 0$).

The collapse duration is also modified by θ_0^*, both when reaching the runout distance t_r and final deposit t_f (see Fig. 9). However, the effect of grain orientation is different in short and tall columns, leading to longer collapse durations in short columns when $\theta_0^* \neq [0°; 90°]$, and the opposite in tall columns, where collapses consistently last longer than in columns with an initially random grain orientation. The longer collapse times in tall columns is asymmetric, leading to longer collapses for $\theta_0^* = -30°$. This behavior is linked to the change in collapse dynamics mentioned above, with the release of stacks of grains sliding on each other. Overall, the variance of the data within collapse repetitions is large, indicating a strong dependency on the initial fabric tensor prior to collapse.

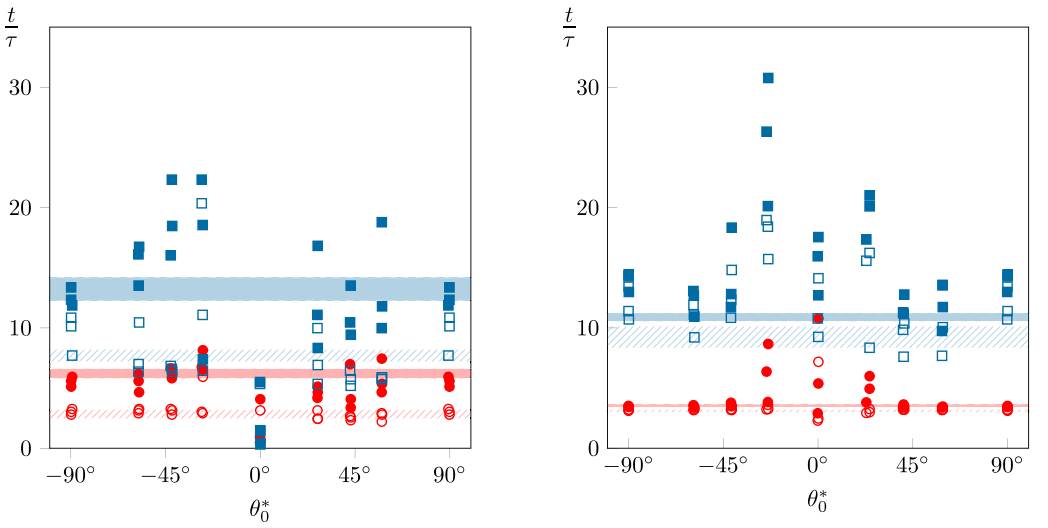

FIG. 9. Dimensionless runout times t_r (empty circles) and final times t_f (solid circles) as a function of the initial main grain orientation θ_0^*. Left: short columns ($H_0/L_0 = 0.5$). Right: tall columns ($H_0/L_0 = 8$). The hatched areas present the range of t_r and the uniform shaded areas indicate the range of t_f for the random initial orientations presented in Fig. 5, with their widths corresponding to two standard deviations. The red circles and blue squares indicate dry and immersed collapses, respectively.

Contrary to the collapse duration, the column runout is slightly affected by θ_0^*, with a marked difference when $\theta_0^* = 0°$ and showing a similar trend for both short and tall columns. (See Fig. 10.) As expected, the observed trend is asymmetric, leading to longer runouts in initially unstable configurations ($\theta_0^* < 0°$) for both dry and immersed collapses. In these configurations the stacked release of grains favors hydrodynamic interactions, propelling the grains further away. Note that for

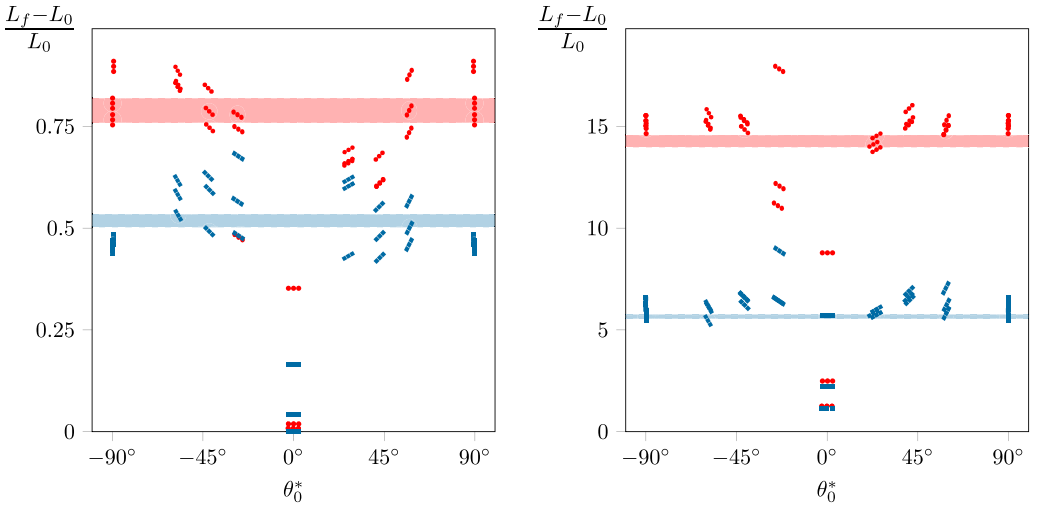

FIG. 10. Effect of initial main grain orientation θ_0^* in the column runout. Left: short columns ($H_0/L_0 = 0.5$). Right: tall columns ($H_0/L_0 = 8$). The shaded areas indicate the mean runout observed in columns with random initial orientations and their widths correspond to two standard deviations. The markers are grains aligned with the prescribed grain orientation. The red and blue colors indicate dry and immersed collapses.

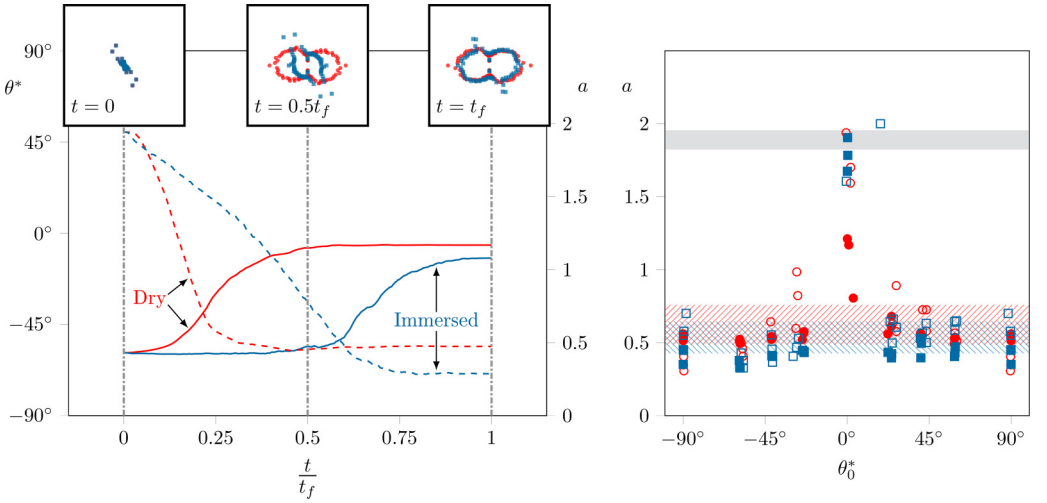

FIG. 11. Left: temporal evolution of the main orientation θ^* (solid) and anisotropy a (dashed) of the orientation distribution for a column with $H_0/L_0 = 8$ and initial grain orientation $\theta_0^* = -60°$. The insets are polar plots of the orientation distribution showing the relative frequency of a given orientation. Right: final a as a function of θ_0^*. Full symbols indicate tall columns and empty ones short columns. The hatched areas indicate the mean value of a for random initial orientations and their widths correspond to two standard deviations. The red circles and blue squares indicate dry and immersed collapses and the gray band corresponds to the mean initial value of $a \pm$ a standard deviation.

columns consisting of an arrangement of nearly vertically oriented grains ($\theta_0^* \approx 90°$) the runout distance is almost that of columns with initially randomly oriented grains. This is found to be associated to rapid changes in the grains' orientation, transitioning to a more uniform distribution and without forming grain stacks.

Tall and short columns share a similar trend in the variation of main grain orientation θ^* and anisotropy a during collapse. In these collapses, θ_0^* and the initial column anisotropy a_0 transition towards a main horizontal orientation and a more uniform fabric. This transition occurs earlier in the collapse in dry columns than in immersed columns, but the final distribution is nearly the same (see instants $0.5t_f$ and t_f in Fig. 11, left). Contrary to randomly oriented immersed columns, the grain main orientation saturates before t_f, reaching a nearly nematic configuration in most cases. The variation of a with θ_0^* shows a peak at $\theta_0^* = 0°$ and then decays in a nearly symmetrical function and towards the fabric anisotropies observed in the initially random collapses (see Fig. 11, right). The peak at $\theta_0^* = 0°$ is expected, since only very few grains collapse, while the attraction to the common value $a \in [0.54 : 0.62]$ indicates a behavior independent of θ_0^*.

In summary, the initial main grain orientation θ_0^* does not have a significant influence on the collapse sequence, the final deposit shape, or the runout distance, but it slightly increases the collapse duration in tall columns. Only orientations close to the horizontal change the general behavior of the column, because of their collective stability. This can be seen in the runout but also in the runout and final times, as well as in the deposit shape.

V. ENERGY CONSIDERATIONS

Previous works have used an energy approach for describing the column collapse sequence and link it with the common features of granular flows [27,33,67–71]. In a column collapse a part of the

initial potential energy E_p transforms into kinetic energy E_k. These can be computed as

$$E_p = \sum_{n=0}^{N} m_n g^* y_n, \tag{7}$$

$$E_k = \overbrace{\frac{1}{2}\sum_{n=0}^{N} m_n u_{nx}^2}^{E_{kx}} + \underbrace{\frac{1}{2}\sum_{n=0}^{N} m_n u_{ny}^2}_{E_{ky}} + \overbrace{\frac{1}{2}\sum_{n=0}^{N} I_n \omega_n^2}^{E_{kr}}, \tag{8}$$

where y_n is the height of grain n, m_n and I_n are its mass and inertia, respectively, and u_n and ω_n are its translational and angular velocities, respectively. It is important to note that the rotational kinetic energy E_{kr} is negligible when compared to the translational components E_{kx} and E_{ky}, as observed in [72] for spherical particles. Therefore, E_{kr} is discarded. Moreover, in immersed cases, the fluid phase also gains kinetic energy E_{kf} in the form

$$E_{kf} = \frac{1}{2}\rho_f \sum_{n=0}^{N_n} v_n^2 V_n \phi_n, \tag{9}$$

where v_n and ϕ_n are the fluid velocity and porosity at node n, respectively, V_n is the volume associated to node n, and N_n is the total number of nodes. This kinetic energy is gradually either dissipated through friction and inelastic collisions in the granular phase or through viscous dissipation in the fluid phase. Then, the total dissipated energy E_d is computed as

$$E_d = E_p(t=0) - E_p - E_k - E_{kf}, \tag{10}$$

assuming that the change in the potential energy of the fluid phase is negligible. These quantities are computed for all columns and traced during collapse.

The temporal evolution of the kinetic energy components and the dissipated energy show a complementary view of the collapse sequence (see Fig. 12). This evolution is similar for initially disordered and ordered columns. Short columns dissipate a smaller fraction of their initial potential energy, as the mobilized material is limited only to a lateral wedge. Also, for short columns, the energy dissipation mainly occurs when the wedge collides with the base. On the contrary, tall columns dissipate a much larger part of their initial potential energy, initiating with a rapid increase in E_{ky}, in line with a predominant free-fall motion, and then transitioning to E_{kx} rising when the grains enter the side-propagation phase. The proportion of dissipated energy is similar to the one for spherical grains [68]. In the immersed case, the energy evolution is less smooth, indicating a nonintuitive coupling between the grains and the fluid. In immersed collapses, the particles fall and transfer an equivalent quantity of energy to the fluid. Part of this energy is dissipated through viscous effects, maintaining the collective motion of grains (e.g., fingerlike structures) and delaying the column motion, in comparison to its dry counterpart. This is because the fluid keeps the kinetic energy for much longer than the grains through a slower viscous dissipation, e.g., $E_{kf} > 0$ at $t = t_f$.

Based on similar observations with the energy approach, the column runout is suggested to depend on its ability to transform the initial potential energy into horizontal kinetic energy [67,68,70,73]. Recent findings on polydisperse column collapses of disks indicate that the runout might be simply controlled by just the front kinetic energy E_k^{fr}. In order to highlight the influence of E_k^{fr} on the column runout, a simple model simplifying the column as a rigid block with mass M and initial horizontal velocity U^{fr} is proposed [27]. Note that E_k^{fr} is much higher than E_{kx} and E_{ky}, as in this simplification the whole column is assumed to move with the front velocity U^{fr} (see Sec. III). The block is subjected to a resistive force $-k\dot{x}$, with k a constant representing the effective viscosity of the granular material. Solving the block's equation of motion $M\ddot{x} = -k\dot{x}$ for an infinite

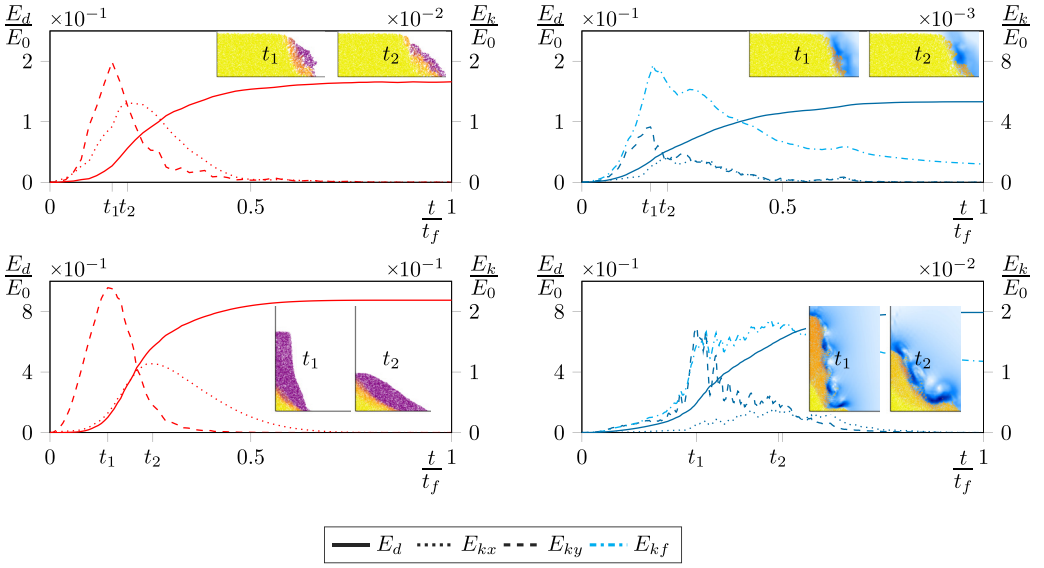

FIG. 12. Temporal evolution of the different forms of energy for initially disordered columns. Top row: for a short ($H_0/L_0 = 0.5$) column in the dry (left) and immersed (right) cases. Bottom row: for a tall ($H_0/L_0 = 8$) column in the dry (left) and immersed (right) cases. The red and blue colors indicate dry and immersed collapses, with cyan corresponding to the fluid phase. The insets show the grain velocity at times t_1 and t_2. The inset color bars are the same as in Fig. 3.

time leads to

$$\frac{L_f - L_0}{L_0} = \frac{\sqrt{2}}{kL_0}\sqrt{M^*}\sqrt{\frac{\rho}{\rho - \rho_f}}\sqrt{E_k^{fr}}, \tag{11}$$

where $M^* = M(\rho - \rho_f)/\rho$ is the column effective mass. From Eq. (11), the following dependence for the runout is suggested [27]:

$$\frac{L_f - L_0}{L_0} \propto \left(\frac{1}{L_0}\right)^{\alpha} M^{*\beta}\left(\frac{\rho}{\rho - \rho_f}\right)^{\gamma} E_k^{fr\,\delta}, \tag{12}$$

with $(\alpha, \beta, \gamma, \delta)$ the exponents controlling the influence of each factor. By a proper fitting of these exponents, they observed a collapse of all data on a single trend, regardless of the level of polydispersity, the column aspect ratio, and the fluid (see the black circles in Fig. 13). The fitted values are $\alpha = 1$ (from the nondimensionalization of the runout), $\beta = 0$ (neglecting the column mass), $\gamma = 1$ (indicating a stronger influence of the fluid), and $\delta = 0.5$.

The data for elongated grains collapses on a single trend for both dry and immersed cases, whatever the column aspect ratio or the initial main grain orientation when the exponents from [27] are used (see the colored symbols in Fig. 13). This trend has a slope close to one (the best fitting line has a slope of 0.995), which is the same as for polydisperse disks. This could indicate that the effect of grain shape on the runout is limited to the prefactor of a power law and not its exponent. Note that with these exponents, Eq. (12) is not dimensionless. The main interest of Eq. (12) is to highlight that this scaling collapses the data with a slope of 1. Nonetheless, it could be made dimensionless by adding a multiplying factor with dimensions of the square root of a typical mass—for example, the one of a single grain. A downward vertical shift with respect to the data for disks corresponding to dividing the data for elongated grains by a constant is observed. This further indicates that the effect of grain shape is on the prefactor of the power law. In other words, for an equal quantity of energy in the column, the runout is reduced for elongated grains. Since the proportion of dissipated

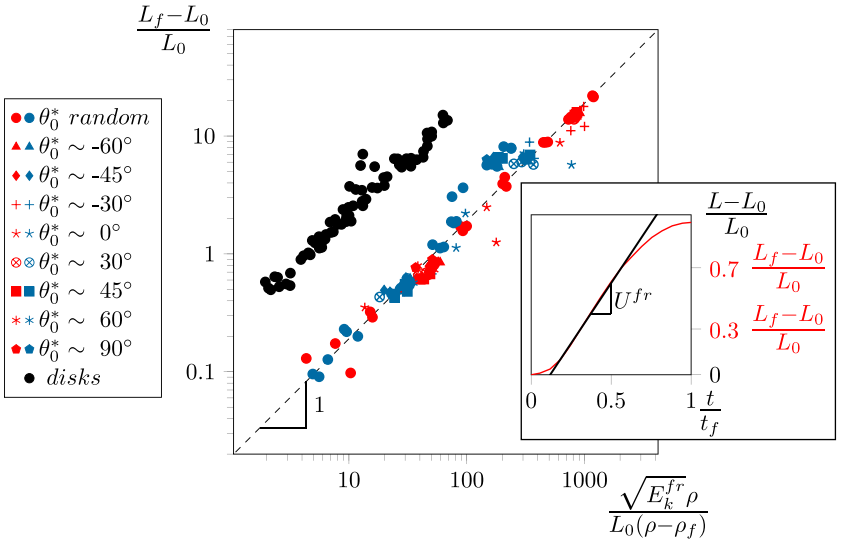

FIG. 13. Runout of the columns scaled with the kinematics of Eq. (12). Data points for short columns with $\theta_0^* = 0^\circ$ were removed as their runout was not relevant. The red and blue colors indicate dry and immersed collapses. Black circles correspond to the data from [27] for polydisperse disks. The dashed line is a guide to the eye with a slope of 1 and a nonzero intercept. The inset illustrates the computation of U^{fr} used to obtain E_k^{fr} for a dry column with $H_0/L_0 = 8$.

energy is equivalent, we suggest that a part of the available energy is consumed by a change in the microstructure of the column, i.e., the orientational rearrangement of the grains. This rearrangement leads to a similar final state for all columns, regardless of the initial main orientation (see Sec. IV). Therefore, the importance of this process should be directly linked to grain properties like grain shape and elongation, although only a weak dependence of the runout on the grain elongation was reported [33]. With this in mind, the factor $\frac{1}{k}$ from Eq. (11), that was discarded in Eq. (12), should be taken into account. The scaling for the runout becomes

$$\frac{L_f - L_0}{L_0} \propto \frac{1}{kL_0} \frac{\rho}{\rho - \rho_f} \sqrt{E_k^f}. \tag{13}$$

The parameter k in the model is linked to the ability of the granular material to flow and reorganize its microstructure. We expect its value to depend on the grain shape, i.e., be more important for grains that have a larger inertia or a better ability to interlock. In that sense, it would be interesting to vary the aspect ratio of the elongated grains or to use other grain shapes. The influence of grain inertia is expected to be easier to determine than the one of their ability to interlock.

VI. CONCLUSIONS

The column collapse of two-dimensional elongated grains was simulated with an unresolved FEM-DEM model both in dry and immersed conditions. The elongated grains were modeled as clusters of disks, facilitating the computation of the fluid-grain interactions in the immersed case. The focus was set on the effect of the column aspect ratio and the initial grain orientation on the collapse dynamics and runout, distinguishing columns with an initial grain orientation that is random or aligned with a given direction.

For randomly oriented grains, the collapse dynamics are found to be analogous to the ones for circular (spherical) grains. Classical power laws were recovered for the runout and final height, with

the fluid phase reducing the runout. The grains align with the flow direction during the collapse, ending up in a nematic configuration.

Concerning columns with a given initial grain orientation, both short (with $H_0/L_0 = 0.5$) and tall (with $H_0/L_0 = 8$) columns were considered. In general, the collapse dynamics and the evolution of the grain orientation distribution are merely unaffected by the initial grain orientation (unless for the extreme cases where the grains are horizontally oriented). The runout is slightly affected, exhibiting an asymmetric increase that is more important for columns with a negative initial grain orientation. Only the collapse duration is increased compared to the case where grains are randomly oriented. The grain orientation transitions to the same nematic state as for columns with randomly oriented grains.

Finally, the evolution of the different forms of energy during the collapse was described and found similar to the one for circular (spherical) grains, with an equivalent proportion of dissipated energy. A scaling of the runout based on the front kinetic energy was used. It collapses the data well on a single line regardless of the column size and initial orientation or the presence of an ambient fluid. When comparing with the data for disks, the runout for a given energy was found smaller for elongated grains. From this, the inclusion of an additional factor in the scaling was suggested in the form of a viscouslike parameter that should account for the grain properties.

Future work should concentrate on identifying the relationship between the additional factor of the front kinetic energy scaling and grain properties. Due to the importance of hydrodynamic interactions with the fluid phase, further efforts could be put into improving their modeling, notably by considering real rodlike grains. Lastly, an extension of the model to three-dimensional configurations should also be interesting.

ACKNOWLEDGMENTS

Computational resources have been provided by the Consortium des Équipements de Calcul Intensif (CÉCI), funded by the Fonds de la Recherche Scientifique de Belgique (F.R.S.-FNRS) under Grant No. 2.5020.11 and by the Walloon Region.

APPENDIX: FLUID SOLVER

The FEM solver uses P1-P1 elements for the sake of computational convenience. Although less accurate, this choice is relevant because the fluid phase is solved on a coarser scale than the granular one. To tackle the unstability which is inherent to P1-P1 elements, a pressure stabilizing/Petrov-Galerkin (PSPG) term and a streamline upwind/Petrov-Galerkin term are added. Finally, a least square on incompressibility constraint term is used for balancing the loss of incompressibility from the PSPG term. More details about the implementation of this method in MIGFLOW can be found in [49].

As said in Sec. II, the fluid-grain interactions are modeled at the disk level and the resulting net torques and forces on the elongated grains are then computed. The interaction with a single disk is modeled as a force which takes into account the drag and pressure gradient contributions. The expression for the drag force on a disk i results from the one for an isolated disk multiplied by a function of the porosity:

$$\mathbf{f}_{d,i} = g(\phi) C \frac{\pi d^2}{4} \left\| \mathbf{u}_i - \frac{\mathbf{v}}{\phi}\bigg|_{\mathbf{x}_i} \right\| \left(\mathbf{u}_i - \frac{\mathbf{v}}{\phi}\bigg|_{\mathbf{x}_i} \right), \tag{A1}$$

with $\mathbf{x}_i$ and $\mathbf{u}_i$ its position and velocity. Dallavalle [52] gives an expression of the drag coefficient suitable for the whole practical range of disk Reynolds numbers Re_d:

$$C = \left(0.63 + \frac{4.8}{\sqrt{\mathrm{Re}_d}} \right)^2, \tag{A2}$$

$$\mathrm{Re}_d = \frac{d\rho_f \phi|_{\mathbf{x}_i}}{\eta} \left\| \mathbf{u}_i - \frac{\mathbf{v}}{\phi}\Big|_{\mathbf{x}_i} \right\|. \tag{A3}$$

The function of the porosity by which to multiply this drag force is of the following form:

$$g(\phi) = \phi^{-\beta}. \tag{A4}$$

The value of $\beta = 1.8$ proposed by Wen and Yu [54], suitable for low and high Reynolds regimes, is used in MIGFLOW [45]. The final expression for the fluid-disk interaction force is the following:

$$\mathbf{f}_i = -\overbrace{V_d \nabla p|_{\mathbf{x}_d}}^{\text{pressure gradient}} - \underbrace{\mathbf{f}_{d,i}}_{\text{drag}}, \tag{A5}$$

with V_d the surface of the disk.

[1] S. Courrech du Pont, P. Gondret, B. Perrin, and M. Rabaud, Granular Avalanches in Fluids, Phys. Rev. Lett. **90**, 044301 (2003).

[2] A. Leonardi, M. Cabrera, F. K. Wittel, R. Kaitna, M. Mendoza, W. Wu, and H. J. Herrmann, Granular-front formation in free-surface flow of concentrated suspensions, Phys. Rev. E **92**, 052204 (2015).

[3] T. T. Vo, S. Nezamabadi, P. Mutabaruka, J. Y. Delenne, and F. Radjai, Additive rheology of complex granular flows, Nat. Commun. **11**, 1476 (2020).

[4] R. Delannay, A. Valance, A. Mangeney, O. Roche, and P. Richard, Granular and particle-laden flows: From laboratory experiments to field observations, J. Phys. D **50**, 053001 (2017).

[5] K. Hutter, Geophysical granular and particle-laden flows: Review of the field, Philos. Trans. R. Soc. A **363**, 1497 (1832).

[6] K. Saleh, S. Golshan, and R. Zarghami, A review on gravity flow of free-flowing granular solids in silos – basics and practical aspects, Chem. Eng. Sci. **192**, 1011 (2018).

[7] M. A. Van der Hoef, M. Ye, M. Van Sint Annaland, A. T. Andrews, S. Sundaresan, and J. A. M. Kuipers, Multi-scale modeling of gas-fluidized beds, Adv. Chem. Engg. **31**, 65 (2006).

[8] E. Azéma and F. Radjaï, Quasistatic rheology, force transmission and fabric properties of a packing of irregular polyhedral particles, Mech. Mater. **41**, 729 (2009).

[9] E. Azéma and F. Radjaï, Stress-strain behavior and geometrical properties of packings of elongated particles, Phys. Rev. E **81**, 051304 (2010).

[10] R. C. Hidalgo, I. Zuriguel, D. Maza, and I. Pagonabarraga, Role of Particle Shape on the Stress Propagation in Granular Packings, Phys. Rev. Lett. **103**, 118001 (2009).

[11] G. Lu, G. R. Third, and C. R. Muller, Discrete element models for non-spherical particle systems: From theoretical developments to applications, Chem. Eng. Sci. **127**, 425 (2015).

[12] T. Pöschel and V. Buchholtz, Static Friction Phenomena in Granular Materials: Coulomb Law Versus Particle Geometry, Phys. Rev. Lett. **71**, 3963 (1993).

[13] T. Börzsönyi, B. Szabó, S. Wegner, K. Harth, J. Török, E. Somfai, T. Bien, and R. Stannarius, Shear-induced alignment and dynamics of elongated granular particles, Phys. Rev. E **86**, 051304 (2012).

[14] S. Wegner, T. Börzsönyi, T. Bien, G. Rose, and R. Stannarius, Alignment and dynamics of elongated cylinders under shear, Soft Matter **8**, 10950 (2012).

[15] G. Lumay and N. Vandewalle, Experimental study of the compaction dynamics for two-dimensional anisotropic granular materials, Phys. Rev. E **74**, 021301 (2006).

[16] G. D. R. Midi, On dense granular flows, Eur. Phys. J. E **14**, 341 (2004).

[17] F. Radjai, J. N. Roux, and A. Daouadji, Modeling granular materials: Century-long research across scales, J. Eng. Mech. **143**, 04017002 (2017).

[18] U. T. Hoang and N. H. Nguyen, Particle shape effects on granular column collapse using superquadric DEM, Powder Technol. **424**, 118559 (2023).
[19] E. Lajeunesse, A. Mangeney-Castelnau, and J. P. Vilotte, Spreading of a granular mass on a horizontal plane, Phys. Fluids **16**, 2371 (2004).
[20] G. Lube, H. E. Huppert, R. S. J. Sparks, and M. A. Hallworth, Axisymmetric collapses of granular columns, J. Fluid Mech. **508**, 175 (2004).
[21] A. Bougouin and L. Lacaze, Granular collapse in a fluid: Different flow regimes for an initially dense packing, Phys. Rev. Fluids **3**, 064305 (2018).
[22] G. Pinzon and M. Cabrera, Planar collapse of a submerged granular column, Phys. Fluids **31**, 086603 (2019).
[23] A. Taylor-Noonan, G. Siemens, M. Cabrera, N. Arpin, F. Parera Morales, and W. Take, Stability of saturated granular columns: Role of stress-dilatancy and capillarity, Phys. Fluids **33**, 033309 (2021).
[24] M. Cabrera and N. Estrada, Granular column collapse: Analysis of grain-size effects, Phys. Rev. E **99**, 012905 (2019).
[25] M. Cabrera and N. Estrada, Is the grain size distribution a key parameter for explaining the long runout of granular avalanches? J. Geophys. Res.: Solid Earth **126**, e2021JB022589 (2021).
[26] L. Lacaze, J. Bouteloup, B. Fry, and E. Izard, Immersed granular collapse: From free-fall to viscous unsteady granular flows, J. Fluid Mech. **912**, A15 (2021).
[27] O. Polanía, M. Cabrera, M. Renouf, and E. Azéma, Collapse of dry and immersed granular columns: A unified runout description, Phys. Rev. Fluids **7**, 084304 (2022).
[28] L. Rondon, O. Pouliquen, and P. Aussillous, Granular collapse in a fluid: Role of the initial volume fraction, Phys. Fluids **23**, 073301 (2011).
[29] N. Estrada, J. Wills, J. Castro, and E. Azéma, Geometric cohesion in granular systems composed of star-shaped particles, VI International Conference on Particle-Based Methods 2019 (unpublished).
[30] K. Karapiperis, S. Monfared, R. B. D. Macedo, S. Richardson, and J. E. Andrade, Stress transmission in entangled granular structures, Granular Matter **24**, 91 (2022).
[31] M. Trepanier and S. Franklin, Column collapse of granular rods, Phys. Rev. E **82**, 011308 (2010).
[32] Y. Zhao, J. Bares, and J. E. Socolar, Yielding, rigidity, and tensile stress in sheared columns of hexapod granules, Phys. Rev. E **101**, 062903 (2020).
[33] H. Tapia-McClung and R. Zenit, Computer simulations of the collapse of columns formed by elongated grains, Phys. Rev. E **85**, 061304 (2012).
[34] R. C. Hidalgo, I. Zuriguel, D. Maza, and I. Pagonabarraga, Granular packings of elongated faceted particles deposited under gravity, J. Stat. Mech.: Theory Exp. (2010) P06025.
[35] A. Jara and M. Cabrera, Planar column collapse of elongated grains, EPJ Web Conf. **249**, 06006 (2021).
[36] G. Lube, H. E. Huppert, R. S. J. Sparks, and A. Freundt, Collapses of two-dimensional granular columns, Phys. Rev. E **72**, 041301 (2005).
[37] E. Boek, P. V. Coveney, H. Lekkerkerker, and P. van der Schoot, Simulating the rheology of dense colloidal suspensions using dissipative particle dynamics, Phys. Rev. E **55**, 3124 (1997).
[38] M. J. Solomon and P. T. Spicer, Microstructural regimes of colloidal rod suspensions, gels, and glasses, Soft Matter **6**, 1391 (2010).
[39] G. Piton, A. R. Ceron Mayo, and S. Lambert, Small-scale modeling of flexible barriers. II: Interactions with large wood, J. Hydraul. Eng. **149**, 04022044 (2023).
[40] I. Schalko, V. Ruiz-Villanueva, F. Maager, and V. Weitbrecht, Wood retention at inclined bar screens: Effect of wood characteristics on backwater rise and bedload transport, Water **13**, 2231 (2021).
[41] I. Schalko, L. Schmocker, V. Weitbrecht, and R. M. Boes, Risk reduction measures of large wood accumulations at bridges, Environ. Fluid Mech. **20**, 485 (2020).
[42] J. J. Major, Pebble orientation on large, experimental debris-flow deposits, Sediment. Geol. **117**, 151 (1998).

[43] P. J. Zrelak, N. M. Pollock, B. D. Brand, D. Sarocchi, and T. Hawkins, Decoding pyroclastic density current flow direction and shear conditions in the flow boundary zone via particle-fabric analysis, J. Volcanol. Geotherm. Res. **402**, 106978 (2020).
[44] The MIGFLOW software, www.migflow.be.
[45] M. Constant, F. Dubois, J. Lambrechts, and V. Legat, Implementation of an unresolved stabilised FEM-DEM model to solve immersed granular flows, Comp. Part. Mech. **5**, 1 (2018).
[46] T. B. Anderson and R. Jackson, A fluid mechanical description of fluidized beds, Ind. Eng. Chem. Fund. **6**, 527 (1967).
[47] M. Jean, The non-smooth contact dynamics method, Comput. Methods Appl. Mech. Eng. **177**, 235 (1999).
[48] J. J. Moreau, Some numerical methods in multibody dynamics: Application to granular materials, Eur. J. Mech. A: Solids **13**, 93 (1994).
[49] M. Constant, N. Coppin, F. Dubois, V. Vidal, V. Legat, and J. Lambrechts, Simulation of air invasion in immersed granular beds with an unresolved FEM-DEM model, Comp. Part. Mech. **8**, 535 (2021).
[50] M. Jean, Méthode de dynamique des contacts, in *Modélisation Numérique Discrète des Matériaux Granulaires*, edited by F. Dubois and F. Radjai (Hermès-Lavoisier, Cachan, 2010), pp. 51–82.
[51] N. Coppin, M. Constant, J. Lambrechts, F. Dubois, and V. Legat, Numerical analysis of the drag on a rigid body in an immersed granular flow, Comp. Part. Mech. **9**, 393 (2022).
[52] J. M. Dallavalle and A. Klemin, *Micromeritics: The Technology of Particles* (Pitman Publishing Corporation, New York, 1943).
[53] J. Richardson and W. Zaki, The sedimentation of a suspension of uniform spheres under conditions of viscous flow, Chem. Eng. Sci. **3**, 65 (1954).
[54] C. Y. Wen and H. Y. Yu, Mechanics of fluidization, Chem. Eng. Prog. Symp. Ser. **62**, 100 (1966).
[55] Y. Jiang, Y. Guo, Z. Yu, X. Hua, J. Lin, C. R. Wassgren, and J. S. Curtis, Discrete element method–computational fluid dynamics analyses of flexible fibre fluidization, J. Fluid Mech. **910**, A8 (2021).
[56] E. Lajeunesse, J. B. Monnier, and G. M. Homsy, Granular slumping on a horizontal surface, Phys. Fluids **17**, 103302 (2005).
[57] C. Meruane, A. Tamburrino, and O. Roche, On the role of the ambient fluid on gravitational granular flow dynamics, J. Fluid Mech. **648**, 381 (2010).
[58] See Supplemental Material at http://link.aps.org/supplemental/10.1103/PhysRevFluids.8.094303 for selected movies of the column collapses of both short and tall columns, in dry and immersed conditions, and with initially ordered and disordered grains. Also included is a csv file with the column data and results for each simulation.
[59] R. M. Iverson, Regulation of landslide motion by dilatancy and pore pressure feedback, J. Geophys. Res.: Earth Surf. **110**, F02015 (2005).
[60] R. Steiner, V. Heller, W. H. Hager, and H. E. Minor, Deflector ski jump hydraulics, J. Hydraul. Eng. **134**, 562 (2008).
[61] L. Staron and E. J. Hinch, The spreading of a granular mass: Role of grain properties and initial conditions, Granular Matter **9**, 205 (2007).
[62] L. Lacaze, J. C. Phillips, and R. R. Kerswell, Planar collapse of a granular column: Experiments and discrete element simulations, Phys. Fluids **20**, 063302 (2008).
[63] N. Schneider, G. Musiolik, J. E. Kollmer, T. Steinpilz, M. Kruss, F. Jungmann, T. Demirci, J. Teiser, and G. Wurm, Experimental study of clusters in dense granular gas and implications for the particle stopping time in protoplanetary disks, Icarus **360**, 114307 (2021).
[64] K. A. Reddy, V. Kumaran, and J. Talbot, Orientational ordering in sheared inelastic dumbbells, Phys. Rev. E **80**, 031304 (2009).
[65] M. Boton, E. Azéma, N. Estrada, F. Radjaï, and A. Lizcano, Quasistatic rheology and microstructural description of sheared granular materials composed of platy particles, Phys. Rev. E **87**, 032206 (2013).
[66] T. Börzsönyi and R. Stannarius, Granular materials composed of shape-anisotropic grains, Soft Matter **9**, 7401 (2013).
[67] L. Jing, G. Yang, C. Kwow, and Y. Sobral, Flow regimes and dynamic similarity of immersed granular collapse: Cfd-dem investigation, Powder Technol. **345**, 532 (2019).

[68] L. Jing, G. Yang, C. Kwok, and Y. Sobral, Dynamics and scaling laws of underwater granular collapse with varying aspect ratios, Phys. Rev. E **98**, 042901 (2018).
[69] L. Staron and E. J. Hinch, Study of the collapse of granular columns using two-dimensional discrete-grain simulation, J. Fluid Mech. **545**, 1 (2005).
[70] V. Topin, Y. Monerie, F. Perales, and F. Radjaï, Collapse Dynamics and Runout of Dense Granular Materials in a Fluid, Phys. Rev. Lett. **109**, 188001 (2012).
[71] R. Zenit, Computer simulations of the collapse of granular columns, Phys. Fluids **17**, 031703 (2005).
[72] S. Utili, T. Zhao, and G. Houlsby, 3d dem investigation of granular column collapse: Evaluation of debris motion and its destructive power, Eng. Geol. **186**, 3 (2015).
[73] G. Yang, L. Jing, C. Kwow, and Y. Sobral, Size efects in underwater granular collapses: Experiments and coupled lattice botlzmann and discrete element method simulation, Phys. Rev. Fluids **6**, 114302 (2021).